IEEE Access
Multidisciplinary | Rapid Review | Open Access Journal

Received July 16, 2021, accepted July 21, 2021, date of publication July 26, 2021, date of current version August 3, 2021.

Digital Object Identifier 10.1109/ACCESS.2021.3100325

Independently Tunable Closely Spaced Triband Frequency Selective Surface Unit Cell Using the Third Resonant Mode of Split Ring Slots

HENRY FABIAN-GONGORA[1], ALEXANDER E. MARTYNYUK[2], JORGE RODRIGUEZ-CUEVAS[2], LOURDES MARTINEZ-LOPEZ[2], ROSALBA MARTINEZ-LOPEZ[2], AND JOSE I. MARTINEZ-LOPEZ[2], (Member, IEEE)

[1]Facultad de Ingenieria, Universidad Autonoma de Campeche, Campeche 24085, Mexico
[2]Division de Ingenieria Electrica, Facultad de Ingenieria, Universidad Nacional Autonoma de Mexico, Mexico City 04510, Mexico

Corresponding author: Jose I. Martinez-Lopez (ismartz@unam.mx)

This work was supported in part by the Programa de Apoyos a Proyectos de Investigacion e Innovacion Tecnologica de la Direccion General de Asuntos del Personal Academico (DGAPA PAPIIT) under Grant IA104921, Grant IN118719, Grant IN118620, and Grant IN119420.

ABSTRACT In this paper, a tunable triband frequency selective surface unit cell based on varactor-loaded split ring slots is presented. By using the third resonant mode, a considerable mutual coupling reduction between adjacent ring slots is obtained ensuring both close band response as well as independent band tuning. Simulated results show the tunable properties of the proposed approach by shifting the three passbands resonant frequencies from 8.368, 10.276, and 12.010 GHz (for the unloaded split ring slots), to 7.732, 9.202, and 10.900 GHz, respectively, when each split ring slot is loaded with a capacitance of 140 fF. Furthermore, the metal shorts that split the ring slots as well as the metal rings located in between the slots are used to build the conducting paths to bias each varactor with minimum disruption in the RF response. A demonstrator based on an X-band diaphragm was designed, fabricated, and experimentally tested. Measured results using a varactor with capacitance range of 30-65 fF show resonant frequencies for the unbiased varactors at 8.53, 9.70 and 11.47 GHz with insertion loss of 1.1, 2.3 and 2.4 dB, respectively, while biasing the diodes at maximum reverse voltages (24 V) provides resonant frequencies at 8.74, 10.03 and 11.77 GHz with insertion loss of 0.8, 1.4 and 1.7 dB, respectively. Frequency shifts of 210, 330 and 300 MHz for the first, second and third resonant frequencies were obtained, respectively. The −10 dB reflection coefficient bandwidths were 495 MHz for the first band, 436 MHz for the second band and 418 MHz for the third band. Close band response is verified obtaining frequency band ratios of 1.18 and 1.14 for the third to the second resonance, and for the second to the first resonance, respectively.

INDEX TERMS Frequency selective surfaces, split ring resonators, mutual coupling.

I. INTRODUCTION

For the last few decades, active frequency selective surfaces (AFSSs) have been investigated due to the ability to reconfigure or tune their response when adapting their characteristics for telecommunications or radar requirements [1], [2]. A passive frequency selective surface (FSS) is a 2-dimensional periodic array of constitutive geometric elements such as metallic features printed on a dielectric slab or apertures etched from a conducting layer with bandstop or bandpass characteristics. Moreover, the addition of active control elements to the FSS allows the reconfiguration of its response to adjust it dynamically to the challenging conditions required in advanced wireless communication systems or radar applications. Therefore, AFSSs are an attractive solution to enhance flexibility, security, and efficiency of the upcoming generations of wireless communication systems [3]–[7].

Recently, multiband FSSs have been developed by virtue of their versatility in multifrequency/multistandard system implementations [8]–[13]. Often, multiband communication systems use channels or services that are closely spaced in frequency. Nowadays multiple X-band

The associate editor coordinating the review of this manuscript and approving it for publication was Davide Comite.

systems are deployed in urban areas. Point-to-point and point-to-multipoint telecommunication systems operate at 10.75-11.25 GHz, weather radars occupy 9.3-9.5 GHz band, and 11.45-11.70 GHz frequency band is destined to ensure downlink in satellite communications. Frequently, urban areas include airports where precision approach radars, air traffic control radars and perimeter security radars also operate at X-band. The main difficulty in this case consists in the fact that the required AFSS should form multiple closely spaced tunable transmission and reflection bands.

Furthermore, with the trend of coexistence and interoperability between different standards and systems, and with the new arrival of 5G systems with their harmonic content, the evident problem of electromagnetic compatibility at X-band can be resolved by using an AFSS that can adapt its frequency characteristics according to the dynamically changing operating scenario. Therefore, the use of electronically reconfigurable FSSs with closely situated passbands and stopbands can be used beneficially in multiband systems preventing Electromagnetic Interference (EMI) between radar and satellite communication antennas [14], interference control in indoor wireless environments [15], and coupling reduction between multiband Multiple-Input Multiple-Output (MIMO) antennas [16].

Different design approaches have been published to obtain FSS with multiple closely spaced bands. These methods include geometries with convoluted patterns, unit cells isolated with a Faraday cage structures, composite resonant elements, and multilayer designs [17]–[24]. The simplest approach is to conform a FSS unit cell with concentric loop geometries, obtaining a multi-resonant element. However, one of the problems of this approach is the strong mutual coupling between the tightly packed loops contained in the unit cell that degrades the FSS performance.

The tunability of AFSS can be obtained by different means. Traditionally, varactor diodes, micro-electromechanical systems (MEMS) and magnetic components have been used as control devices to modify the scattering parameters of the AFSS [25]–[27]. For faster response and better reliability, electronic devices are usually preferred over the other technologies. Therefore, varactor diodes embedded in a multiband FSS unit cell have been successfully employed as tuning devices to obtain a tunable multiband response.

Split rings and split ring slots have been used to develop tunable microwave circuits [28], [29], compact metamaterial structures [30], [31], as well as single band tunable FSSs [32]. Also, concentric split ring slots have been used to obtain a tunable dual-band AFSS. In [33], a varactor-loaded tunable dual band AFSS using the first resonant mode of complementary split rings was presented. This approach based on the fundamental resonant mode is convenient when the physical separation of the two slots is not too small, which corresponds to two passbands that are not closely located in the frequency domain. However, when the proximity of the slots reduces, a considerable mutual coupling between ring slots arises thus preventing the close separation between the resonant frequencies of the multiband FSS. Other independently tunable multiband FSS have been proposed in the literature. In [34] a Terahertz FSS with three passbands based on a Hybrid Metal-Graphene structure that can be tuned by inserting graphene strips between metal patches was presented. The main drawback of this approach is the fabrication complexity. Next, an AFSS with a unit cell containing two cross strips with different dimensions encircled with high pass grids was proposed in [35] to obtain two independently tunable passbands. Later, a varactor-loaded dual-band AFSS based on cross-diagonals terminated with square loops was reported in [36]. This FSS exhibits independent tuning of the two stopbands with wideband response.

Further from the previous efforts, this paper proposes two main advances. The first one is the usage of the third resonant mode of the split ring slot resonators instead of the fundamental resonant mode. This third mode allows the reduction of the mutual coupling between the densely packed resonators to ensure closely spaced resonant frequencies with the capability of independent tuning. The second development is the design of the biasing network needed to independently control the three active devices in the unit cell with low disruption in the microwave regime. As a result, a triple-band AFSS unit cell based on varactor-loaded split ring slots, optimized for independent band tuning operation and close band response, is presented. To the best of the authors' knowledge, this is the first time that an independent tunable triband FSS unit cell with close band response is presented. The proposed geometry allows the efficient loading of the AFSS unit cell using only one varactor for each ring slot and is also well-suited for integration with the low disruptive bias circuits required to control the tunable response of each band.

A possible scenario for the proposed AFSS includes the situation when a perimeter security airport radar operating within 9.75-10.00 GHz frequency range and an air traffic control radar occupying 8.5-8.75 GHz frequency range share the same airport tower. The nearby urban area with high-rise buildings extensively uses X-band point-multipoint links deployed at 10.75-11.25 GHz, causing interference for the tower radars operations. Additionally, weather radar operating at 9.3-9.5 GHz is used for local weather forecasting and severe weather warnings. Even typical for urban areas, L-band 4G LTE mobile communication systems generate spurious interference at X-band affecting the radar data quality of X-band radars [37]. Within the above-mentioned complicated and highly dynamic scenario, the main task for the proposed AFSS is to ensure narrow electronically adjustable transmission bands within 8.5-8.75 GHz and 9.75-10.00 GHz for tower radars while dynamically providing deep reflection bands for weather radar carriers and interferences caused by point-multipoint links at 9.3-9.5 GHz and 10.75-11.25 GHz frequencies, respectively. Moreover, the proposed AFSS ensures tunable narrow transmission bands for communication satellites operating at 11.45-11.7 GHz frequency bands.

This paper is organized as follows: The operation principle of the triband AFSS is described in section II. The design

methodology of an X-band AFSS unit cell is presented in section III. The fabrication process is explained in Section IV, while section V details the experimental validation for different biasing conditions that enable different operating modes. Finally, section VI presents the conclusion and remarks.

II. PRINCIPLE OF OPERATION

The unit cell of the proposed AFSS is presented in Fig. 1(a). In this design, we use three concentric ring slots with a metallic short that splits each ring slot to obtain three operating bands. It consists of three concentric split ring slot resonators with medium radii of r_1, r_2 and r_3, and slot width of w. The orientation of the metal short in each ring slot is alternated by 180° with respect to the nearest ring. The angular positions of the shorts of the outer, middle, and inner ring slots are located at 90°, 270° and 90° with respect to the x- axis, respectively. Each ring slot has one metal short of width g and is loaded with a varactor diode Di, where i is an index to distinguish each diode. The FSS elements are located at the nodes of a rectangular lattice with periods b and d in the x and y directions, respectively. A dielectric slab with dielectric permittivity of ε_r and thickness of h is used to support the AFSS as shown in Fig. 1(b).

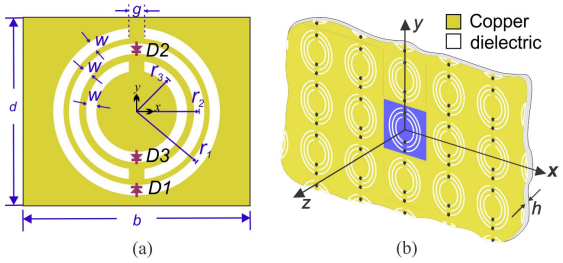

FIGURE 1. AFSS based on three concentric complementary split rings. a) Unit cell geometry, and b) 2-dimensional AFSS.

A. MUTUAL COUPLING OF CLOSELY-PACKED CONCENTRIC RING SLOTS

Initially, to illustrate the effect of the strong mutual coupling of the fundamental resonant modes in the nested unsplit ring slots, the unloaded FSS with only one unsplit ring slot resonator per unit cell was analyzed. Then, the reflection coefficient of three different FSS unit cells denoted by *FS1, FS2* and *FS3* containing a single unsplit resonator with medium radii of the slots of 4.8, 4.25 and 3.7 mm, respectively, and slot width of 0.3 mm were simulated. All unit cells with $b = d = 10.8$ mm are patterned on a substrate with dielectric permittivity of 10.2 and thickness of 0.13 mm. This infinite periodic structure is free of grating lobes up to 13.9 GHz. The reflection coefficient for the scattering of the y- polarized normally-incident wave on the infinite FSS is evaluated using the full-wave frequency-domain solver within CST Studio Suite. The scattering of the wave reveals the appearance of the resonant frequencies at 6.41 GHz for *FS1*, 7.65 GHz for *FS2*, and 8.93 GHz for *FS3* as shown in Fig. 2. Therefore,

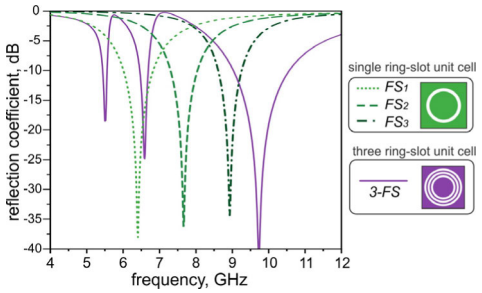

FIGURE 2. Simulated reflection coefficient magnitudes for three FSS unit cells with single ring slots and a FSS unit cell with three concentric ring slots.

the ratio between the lowest and the highest resonant frequencies is 1.39, which approximately corresponds to the ratio of 1.30 between the medium radii of the largest and the smallest rings. However, the simulation of the FSS with a unit cell that contains all three unsplit resonators for the above-mentioned medium radii (*3-FS*) reveals that the resonant frequencies have been changed. These new resonant frequencies are 5.51, 6.57 and 9.70 GHz. The resulting ratio between the highest and the lowest frequencies now is 1.76, that is significantly higher as compared with the calculated ratio for the FSSs with single resonators. This fact reveals a severe mutual coupling between all three closely-packed ring slot resonators. It is recognized from the theory of coupled circuits that strong mutual coupling between two resonant LC circuits with slightly different resonant frequencies result in a transmission characteristic with two maximums spreading farther apart, and the difference between the frequencies of these maximums is substantially larger than the difference between the self-resonant frequencies of the uncoupled resonators.

Thus, the change in f_{max}/f_{min} ratio can be used to evaluate the mutual coupling between resonators. The main effect of the coupling of these contiguous ring slots is that the separation between their resonant frequencies increases, complicating the close-band design.

B. MUTUAL COUPLING OF CLOSELY-PACKED CONCENTRIC SPLIT RING SLOTS, FUNDAMENTAL AND THRID ORDER RESONANT MODES

Next, the mutual coupling of closely-located split ring slots is studied. To observe the effect of the mutual coupling one can compare the case of unit cells with a single split ring slot with the response of the unit cell with three concentric rings slots. Thus, three FSSs denoted by *sFS1, sFS2* and *sFS3* with unit cells containing a single split ring slot resonator with medium radii of 4.8, 4.25 and 3.7 mm, respectively, slot width w of 0.3 mm, and metal short width g of 0.3 mm have been simulated assuming the vertical polarization of the incident wave. The simulation of the infinite FSSs in a wide frequency range shown in Fig. 3 reveals two resonant frequencies for each FSS corresponding to the fundamental (low resonant frequencies) and the third (high frequencies)

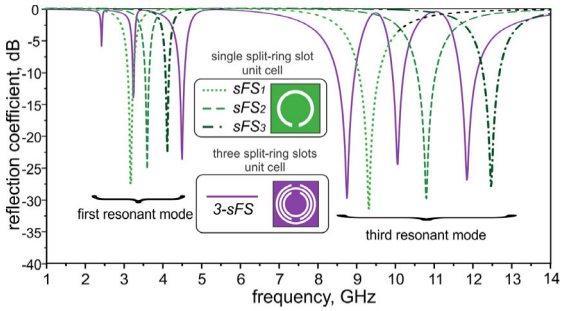

FIGURE 3. **Simulated reflection coefficient magnitudes for three FSS unit cells containing a single concentric unsplit ring slots and a FSS unit cell having three concentric split ring slots.**

resonant modes. These resonant frequencies are respectively 3.15 and 9.26 GHz for *sFS1*, 3.6 and 10.8 GHz for *sFS2*, and 4.12 and 12.46 GHz for *sFS3*. As expected, the resonant frequencies of the third modes are approximately three times higher than the resonant frequencies corresponding to the fundamental resonant modes for all FSS containing a single ring slot resonator with one short. Furthermore, the ratios between the highest and the lowest resonances for the third resonant mode and the first resonant modes are 1.35 and 1.31, respectively, in accordance with the ratio between medium radii of the largest and smallest rings as shown in Table 1.

TABLE 1. **Frequencies and frequency ratios of different FSS unit cells.**

FSS Unit Cell	f_1 [GHz]	f_2 [GHz]	f_3 [GHz]	f_2/f_1 [GHz]	f_3/f_2 [GHz]	f_3/f_1 [GHz]
FSi	6.41	7.65	8.93	1.19	1.17	1.39
3-FS	5.51	6.57	9.70	1.19	1.48	1.76
sFSi (1st mode)	3.15	3.60	4.12	1.14	1.14	1.31
sFSi (3rd mode)	9.26	10.8	12.46	1.17	1.15	1.35
3sFS (1st mode)	2.42	3.25	4.51	1.34	1.39	1.86
3s-FS (3rd mode)	8.75	10.06	11.85	1.15	1.18	1.35

The addition of a single short to the ring slot leads to the reduction of the resonant frequency of the fundamental mode approximately by half [38]. For this fundamental mode, a perimeter of the ring slot is approximately equal to $\lambda/2$, where λ is the wavelength at the resonant frequency. The resonant frequency of the second resonant mode is the same as the resonant frequency of the fundamental mode of the unsplit ring slot resonator. For this case, the maximum of the electric field in the ring slot appears on the orthogonal axis with respect to the short of the ring slot and the perimeter of the ring slot is approximately equal to λ.

The third resonant mode of the ring slot resonator with one short corresponds to the case when the perimeter of the ring slot is approximately equal to $3\lambda/2$ at the correspondent resonant frequency. Therefore, for a linearly polarized normally-incident wave with electric vector aligned to the short, the presence of a single metal short also leads to the appearance of an additional transmission band with resonant frequencies increased by a factor 1.5 as compared with resonant frequencies corresponding to the fundamental mode of the unsplit ring slot resonators.

Finally, the unit cell with three concentric split ring slots (*3sFS*) with medium radii of 4.8, 4.25 and 3.7 mm is analyzed. The simulated characteristic reveals two groups of three resonant frequencies as shown in Fig. 3. The lower frequency group corresponds to the fundamental resonances of the coupled system of split ring slot resonators. The resonant frequencies in the lower frequency group are 2.42, 3.25 and 4.51 GHz. The ratio between the highest and the lowest frequency is 1.86, which is almost the same as in the case of the FSS with the unit cell that contains three unsplit ring slot resonators. Fig. 4 shows the electric field and surface current distributions in the FSS unit cell for the first resonant mode. One can still observe a strong mutual coupling between the split ring slots as the electric field and surface currents are heavily excited in more than one ring slot.

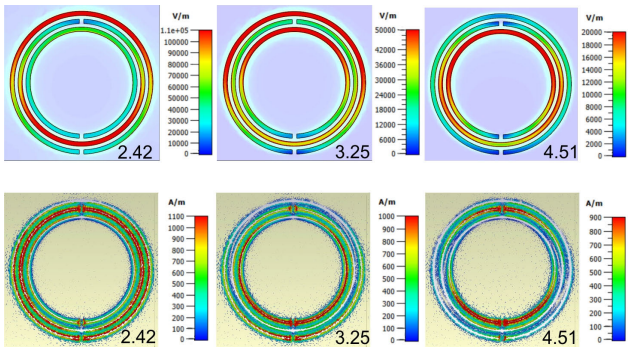

FIGURE 4. **Electric field intensities (upper) and surface current densities (bottom) of the three concentric split ring slots for the fundamental resonant mode at 2.42, 3.25 and 4.51 GHz.**

The resonant frequencies of the higher frequency group, corresponding to the third resonant mode, are 8.75, 10.06 and 11.85 GHz. The ratio between the highest and the lowest frequencies is 1.35 and corresponds to the ratio between the medium radii of the largest and the smallest ring slot resonators, which clearly indicates a strong suppression of the mutual coupling. Therefore, by using the third resonant modes, instead of the fundamental modes, the frequency band ratios of two adjacent split ring slot resonators are small, allowing their resonances to be closely spaced. All these previous results are summarized in Table 1.

The moderate (less than 10%) decrement in the resonant frequencies as compared with the resonant frequencies calculated for single split slot resonators can be explained from the modified geometries. For instance, the inductances in the equivalent circuits are higher for the unit cell with three resonators due to the thinner metal features. Thus, it can be concluded that the usage of the third resonant mode in the coupled system of split ring slot resonators ensures a significant suppression of the mutual coupling.

This effect can be also explained from the particularities of the electric field distribution in the system of split ring slot resonators with opposite positions of the shorts: the maxima of the electric field in the resonating ring correspond to the minima of electric field in the adjacent non-resonating split rings as shown in Fig. 5. One can observe, for the outer split

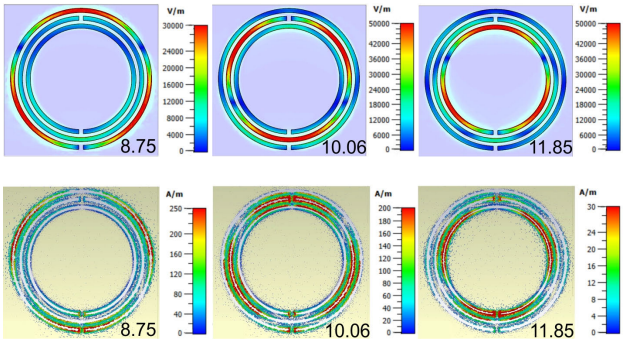

FIGURE 5. Electric field intensities (upper) and surface current densities (bottom) of the three concentric split ring slots for the third resonant mode at 8.75, 10.06 and 11.85 GHz.

ring slot, three maxima of the electric field located at 90°, 210° and 330° with respect to the x-axis, while for the middle ring the three maxima of the electric field are located at 30°, 150° and 270°.

The effective redistribution of the resonant surface currents at the vicinity of the shorts in distant regions within the unit cell is also observed. The surface electric currents are displayed in Fig. 5 for each of the resonant frequencies of the multiband response. One can observe that the concentrations of the surface currents along the borders of the metal shorts occur at different locations in the unit cell. Indeed, the electric current for each resonant frequency is concentrated in three sections: one near the metal shorts and the other two at approximately ±120° apart from the angular position of the short. Therefore, by alternating the angular positions of the metal shorts in two contiguous ring slots by 180° (locating the shorts on the opposite sides of the two contiguous ring slots), a negligible mutual coupling is effectively obtained, enabling closely spaced resonant frequencies. The above-mentioned effect has been used in this work to obtain an independent tuning of the closely spaced resonant frequencies with the help of varactors installed on the opposite side of the short that splits each ring slot.

For the case of y- polarization of the incident wave and the third resonant mode of the AFSS unit cell, the resonant frequencies are shifted upward and, due to the decrease of the mutual coupling, the frequency spacings between the new resonant frequencies are reduced as compared to the case of the three unshorted ring slots. As the electric and magnetic fields related to each resonance are now spatially separated within the unit cell, independent band frequency tuning can be obtained by reactive loading of each ring slot with a varactor diode. It is important to mention that the metal shorts splitting each ring slot also provide the convenient conducting paths for the integration of the low-disruptive DC bias circuits required to bias each varactor diode independently.

III. TUNABLE FSS UNIT CELL IN X-BAND

A triband FSS unit cell based on loaded split ring slots to operate in X-band was analyzed. The design of the FSS unit cell starts by optimizing the radii of the split ring slots to ensure close band response with low insertion loss in the transmission bands and high isolation in the reflection bands. The resonant frequencies of the outer, middle, and inner ring slots correspond to the lower, middle, and upper bands of the design. Next, each ring is loaded by an impedance that corresponds to a capacitance C_v connected in parallel with a resistance R. This capacitance is varied to analyze the tuning properties of the FSS unit cell. In this design, a dielectric substrate with a dielectric permittivity of 11.2, a dielectric thickness of 130 μm, and a loss tangent of 0.0023 was considered. Note that the high value of dielectric permittivity is used to miniaturize the unit cell. These optimizations were completed using the frequency-domain solver in CST Studio Suite®. The sizes of the optimized unit cell geometry are given by $b = d = 10.16$ mm, $r_1 = 4.70$ mm, $r_2 = 3.40$ mm, $r_3 = 3.95$ mm, $g = 0.3$ mm, and $w = 0.2$ mm. The optimized infinite periodic structure is free from grating lobes up to 14.76 GHz.

The simulation calculates the scattering of the normally-incident y-polarized wave on the AFSS assuming unit cell boundary conditions in the x- and y- directions. Initially, one can consider that three loading capacitances vary simultaneously with the same rate. The computed reflection and transmission coefficient magnitudes for different loading cases ($R = 10$ kΩ and C_v varying from 0 to 140 fF) are shown in Fig. 6(a)-(b), respectively. One can observe that three resonances located at 7.732, 9.202 and 10.900 GHz can be tuned up to 8.368, 10.276 and 12.010 GHz by varying the capacitances from 140 to 0 fF. The frequency variation of the first, second and third resonances are 636, 1074, and 1110 MHz, respectively, corresponding to tuning ranges of 7.9 %, 11 %, and 9.7%, respectively.

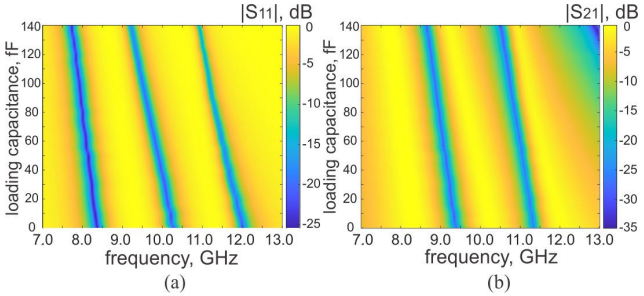

FIGURE 6. Simulated a) reflection, and b) transmission coefficient magnitudes considering a variable capacitance (0 to 140 fF) in the loading impedance for the case of synchronized tuning.

Secondly, the independent tuning of the FSS unit cell was evaluated. The simulations were performed varying only one impedance of the tunable split ring slot while setting the other two untuned split ring slots to 0 fF. Figs. 7(a)-(b), 8(a)-(b) and 9(a)-(b) show the reflection and transmission coefficient magnitudes for the cases of the independent tuning of the outer, middle, and inner split ring slots, respectively. The independent tunable properties of the third resonant mode are observed. Note that these tuning ranges do not affect the contiguous passbands, in other words, the shifts in the

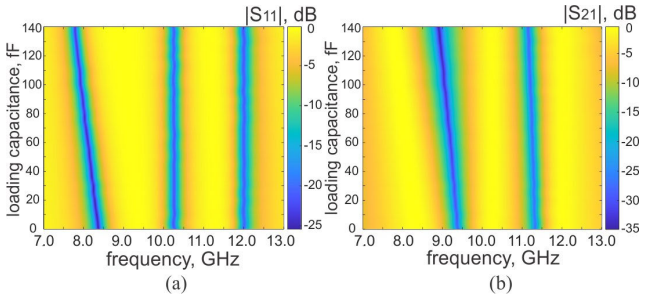

FIGURE 7. Simulated a) reflection, and b) transmission coefficient magnitudes considering a variable capacitance (0 to 140 fF) in the loading impedance for the case of independent tuning of the outer split ring slot.

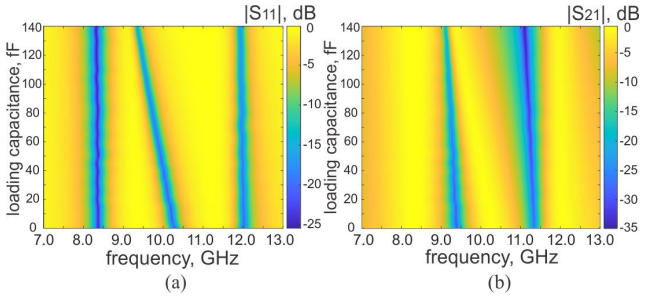

FIGURE 8. Simulated a) reflection, and b) transmission coefficient magnitudes considering a variable capacitance (0 to 140 fF) in the loading impedance for the case of independent tuning of the middle split ring slot.

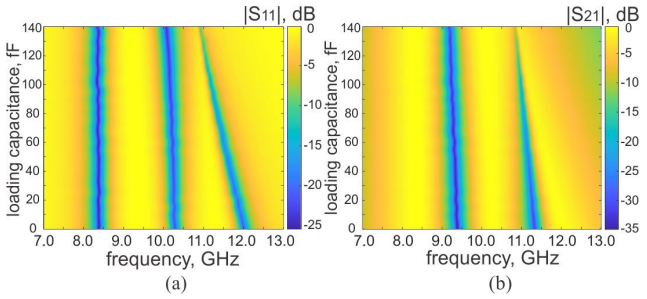

FIGURE 9. Simulated a) reflection, and b) transmission coefficient magnitudes considering a variable capacitance (0 to 140 fF) in the loading impedance for the case of independent tuning of the inner split ring slot.

resonant frequencies do not overlap or interfere with the other two operating bands.

A. EQUIVALENT CIRCUIT MODEL

Based on the previous results, an equivalent electrical circuit model (ECM) for the third resonant mode is obtained. Due to the electric field intensities and surface current distributions observed at resonant frequencies in Fig. 5, each loaded split ring slot can be modeled as shown in Fig. 10(a). The inductances L_r and L_l are due to the electric currents that flow at the right and left part of the split ring slot, respectively, while the inductance L_s is due to the electric current that flow through the metal short that splits the slot. The upper inductance L_u and lower inductance L_d exist due to the currents flowing in

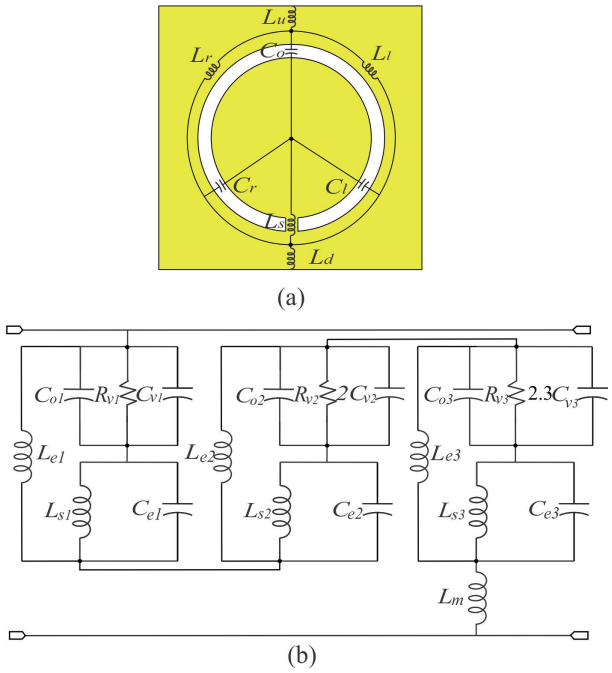

FIGURE 10. Third resonant mode's equivalent circuit model of the FSS unit cell. a) schematic of the FSS unit for an unloaded single split ring slot, and b) ECM of the loaded three band FSS unit cell.

the metal at the upper and lower part of the unit cell. The capacitances C_o, C_r, and C_l are due to the electric field stored in the slot with maximum intensities at the angular positions of 90°, 210° and 330° from the x-axis, respectively. Due to the high reduction of the coupling between adjacent split ring slots, one can approximate the total ECM of the three concentric loaded split ring slots by connecting in series three uncoupled circuits as shown in Fig. 10(b). Considering the symmetry of the unit cell, L_e is the parallel connection of L_r and L_l, while C_e is the parallel connection of C_r and C_l. L_m is the series equivalent of L_u and L_d. In this circuit, the model of a varactor diode that consists of a parallel connection of a capacitance C_v and a resistor R, is connected in parallel to the capacitance C_o. The values of these parameters were fine-tuned using ADS Keysight Pathwave®. The parameters of the ECM for the X-band FSS in free space are given by $C_{o1} = 700$ fF, $C_{o2} = 1010$ fF, $C_{o3} = 1323$ fF, $C_{e1} = 18$ pF, $C_{e2} = 14$ pF, $C_{e3} = 13.2$ pF, $L_{e1} = 0.540$ nH, $L_{e2} = 0.256$ nH, $L_{e3} = 0.148$ nH, $L_{s1} = 0.160$ nH, $L_{s2} = 0.150$ nH, $L_{s3} = 0.150$ nH, $L_m = 0.150$ nH, $R_{v1} = 2.9$ kΩ, $R_{v2} = 1.6$ kΩ, and $R_{v3} = 1.2$ kΩ. Fig. 11(a)-(b) show the comparison of the reflection coefficient magnitudes obtained with the full-wave solver and the ones obtained by the ECM considering the maximum (65 fF) and minimum (30 fF) values of the varactor diode used in the demonstrator, respectively. A good agreement can be observed.

The scattering of the *TE* incident plane wave with oblique angular incidence is also studied. The reflection coefficients for incident azimuthal angle $\phi_0 = 0°$, $C_v = 65$ fF, and different incident elevation angles θ_0 are analyzed and shown

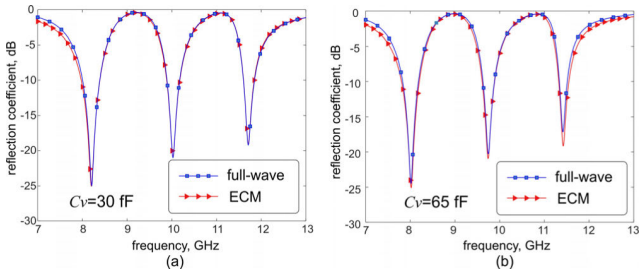

FIGURE 11. Simulated reflection coefficient magnitudes for the full-wave solver and the ECM considering the a) maximum value (65 fF), and b) minimum value (30 fF) of the varactor's capacitance used in the demonstrator.

in Fig. 12. One can observe good angular stability for incident elevation angles up to 30°.

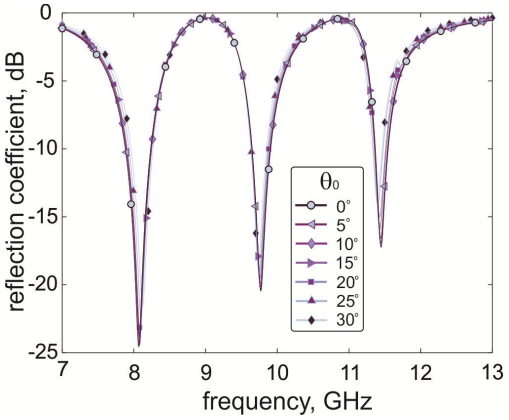

FIGURE 12. Simulated reflection coefficient for different incident elevation angles of θ_0. The azimuthal angle φ_0 is 0° and $C_V = 65$ fF for all cases.

IV. ACTIVE FSS UNIT CELL FABRICATION

An active diaphragm containing a varactor-loaded three concentric complementary split ring slots was designed, fabricated, and mounted at the cross-section of a WR-90 waveguide for experimental validation of the operation principle using the waveguide simulator method. Therefore, the AFSS unit cell dimensions are modified to match the dimensions of the standard WR-90 rectangular waveguide. Thus, $b = 22.86$ mm and $d = 10.16$ mm correspond to the new FSS unit cell sizes. The geometry sizes of the ring slots are the same as the ones optimized in section III. The concentric split ring slots were etched on the copper cladding of a microwave friendly substrate. The 0.130 mm-thick Rogers ®RO3010 substrate ($\varepsilon_r = 11.2$, $\tan\delta = 0.0023$) was used for the diaphragm fabrication. To ensure an independent tuning for each of the ring slots, individual bias lines were formed to bias each varactor diode using a metal-insulator-metal fabrication process based on Benzocyclobutene (BCB) [39]. This process has demonstrated a low-disruptive effect in the biasing of the active devices due to the very low impedance of the bias lines. Note the that the inner metal rings that separate the split ring slots were used as conducting paths to fabricate the bias lines on top of them. The process consists of depositing and patterning a 5 μm-thick dielectric layer of photo definable BCB above the substrate's copper cladding (1st BCB layer). Next, DC bias lines with triangular open-ended stubs are formed by the deposition of a copper film (1st copper layer) with thickness of 1 μm with the subsequent patterning by wet chemical etching. Each of the triangular open-ended stubs were designed to ensure a short circuit between the varactor's anode and the edge of the ring slot at the center frequencies of the corresponding passband. On the other hand, all the varactor cathodes are connected to ground, allowing the connection of each varactor in parallel to the respective ring slot. The GaAs tuning varactor diodes MA46H146 from MACOM® were used to load all ring slots of the diaphragm. External connections to provide independent DC voltage to each diode were made to ensure the tunable multiband operation. The schematic of the active diaphragm indicating the DC bias lines for each varactor and a photograph of the active diaphragm mounted on the waveguide simulator are shown in Fig. 13(a) and (b), respectively.

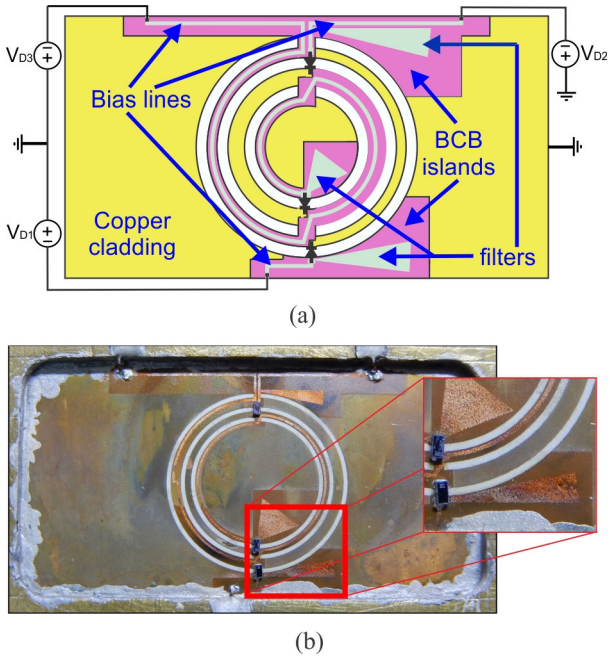

FIGURE 13. Active diaphragm. a) Schematic of the diaphragm for the waveguide simulator indicating the DC bias lines, and b) fabricated diaphragm mounted on the WR-90 waveguide cross-section.

This unit cell can be interwoven with other FSS cells in a two-dimensional periodic array as shown in Fig. 14 by adding second layers of BCB and copper. Bias lines made of copper can be deposited on top of the first BCB layer to provide the required DC voltages (V_{D1}, V_{D2} and V_{D3}) for the varactor diodes connected in parallel in each row. For illustration purposes, three diverse shades of green are used in Fig. 14 to differentiate the lines to bias the inner, middle, and outer ring slots, even though all these lines correspond

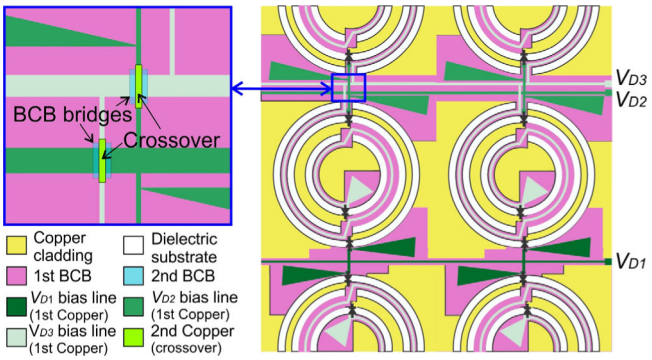

FIGURE 14. Biasing network design of interwoven FSS unit cells in a periodic 2-D array to independently tune each passband.

to the first deposited copper layer. To avoid a short circuit between bias lines, BCB bridges (2nd BCB layer) with a top metal strip (2nd copper layer) can be used for crossover using the same process as the one described in [40].

V. EXPERIMENTAL VALIDATION

The experimental validation was made using the waveguide simulator technique (WS) [41], [42]. This method provides the advantage of testing a single unit cell of the AFSS considering that the metal waveguide walls provide the environment of an infinite array. Therefore, the scattering of the TE_{10} wave on the active diaphragm installed at the WS is analogous to the scattering of a two *TE* Floquet waves with an angle of incidence $\theta_0 = \arcsin(\lambda/2b)$ on the equivalent infinite AFSS whose symmetry planes are correctly considered in the WS. Some of the advantages of this method, as it mirrors the active diaphragm to form an infinite array of unit cells, are that it allows one to ignore the diffraction on the borders, the difference between elements due to fabrication errors, and the spread in values of the control devices that worsen the performance of finite size AFSS.

The experimental setup used to characterize the active diaphragm consists of a vector network analyzer (VNA) connected to the WS to measure the scattering parameters. The DC biasing is ensured through three independent DC power supplies connected respectively to each varactor diode. A photograph of the experimental setup is shown in Fig. 15(a-b). To evaluate the behaviour of the AFSS, three operating modes were analyzed: synchronized band tuning, independent band tuning and two-band tuning. Thus, various reverse bias voltages V_{Di} were applied to the diodes in the fabricated diaphragm to evaluate the tuning of the corresponding resonant frequencies. The scattering parameters $|S_{11}|$ and $|S_{21}|$ were measured for the three operating modes. In the first one, the same varying bias voltages were applied to all three diodes. In the second one, only the bias voltage of one diode was varied and the other two bias voltages were kept constant at $V_D = 0$ V. In the third case, the voltages of two diodes were locked and varied while keeping the third diode voltage constant at $V_D = 0$ V. The maximum capacitance value of

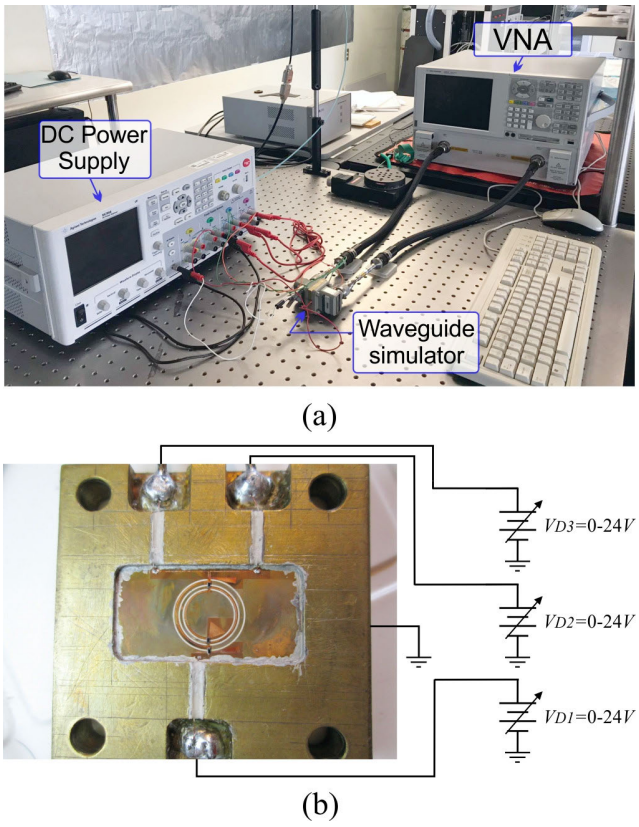

FIGURE 15. Experimental setup. a) Photograph of the setup, and b) fabricated diaphragm installed in the waveguide simulator.

the varactor diode is 65 fF and is ensured for $V_D = 0$ V, while the minimum capacitance value is 30 fF corresponding to the maximum reverse voltage of $V_D = 24$ V.

A. SYNCHRONIZED BAND TUNING

The measured scattering parameters $|S_{11}|$ and $|S_{21}|$ of the active diaphragm for the case of the same reverse bias voltages applied for all three diodes are shown in Fig. 16. To observe this synchronized tuning, the bias voltages of 0, −2, −6 and −24 V were applied. One can observe a resonant frequency tunable range of 210, 330 and 300 MHz for the first, second and third resonant frequencies, respectively. The −10 dB reflection coefficient bandwidths, obtained when the reverse bias voltages were swept from the minimum to the maximum voltages, were 495 MHz for the first operating band, 436 MHz for the second band and 418 MHz for the third band. Higher insertion loss was also observed at low reverse bias voltages as expected for varactor diodes. Table 2 presents the measured insertion loss for the case of the unbiased diodes at 0 V and the reverse-biased diodes at 24 V that correspond to the highest and lowest varactor diode capacitance, respectively. The frequency ranges with isolation levels better than 15 dB and 20 dB for each of the two rejection bands are provided in Table 3. To visualize better in the figure the aforementioned bands, the −10 dB reflection coefficient bandwidths are shaded in blue, while

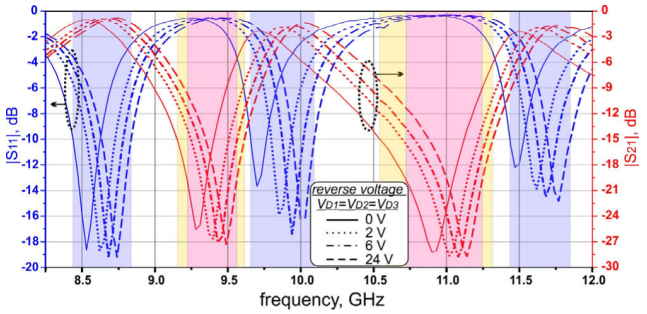

FIGURE 16. Measured scattering parameters of the active diaphragm at the WS for synchronized band tuning.

TABLE 2. Measured values of insertion loss at minimum and maximum reverse bias voltages, corresponding to 65 and 30 fF of the varactor's capacitance, respectively.

Pass-band	Resonant frequency at 0V [GHz]	Insertion loss at 0V [dB]	Resonant frequency at 24V [GHz]	Insertion loss at 24V[dB]	-10 dB Ref. Coef. BW. [MHz]
Lower	8.53	1.1	8.74	0.8	495
Middle	9.70	2.3	10.03	1.4	436
Upper	11.47	2.4	11.77	1.7	418

TABLE 3. Measured values of isolation at minimum and maximum reverse bias voltages, corresponding to 65 and 30 fF of the varactor's capacitance, respectively.

Rejection band	15 dB isolation freq. range at 0V [GHz]	15 dB isolation freq. range at 24V [GHz]	20 dB isolation freq. range at 0V [GHz]	20 dB isolation freq. range at 24V [GHz]
First	9.16-9.42	9.35-9.62	9.23-9.35	9.42-9.56
Second	10.53-11.13	10.88-11.32	10.73-11.05	11.00-11.25

the rejection bands with isolation levels better than 15 dB and 20 dB are shaded in yellow and red, respectively.

B. INDEPENDENT BAND TUNING

The second operating mode considers that only one of the three resonant frequencies needs to be tuned. For the resonant frequencies that are not tuned, the reverse bias voltages for the corresponding diodes are set to 0 V. On the other hand, five different reverse bias voltages equal to 2, 4, 6, 12 and 24 V were applied to the diode that corresponds to the tuned band. Fig. 17(a)-(c) show the magnitudes of the transmission and reflection coefficients for the case of tuning only one resonant frequency while the other two frequencies remain untuned. It is observed that the tuning of the selected resonant frequency does not affect either the resonant frequencies or the bandwidths of the other two untuned bands.

C. TWO-BAND BAND TUNING

The third operating mode affirms that two resonant frequencies are simultaneously tuned while the remaining resonant frequency is not tuned. The voltages of the two reverse-biased diodes are set to 2, 6 and 24 V, while the voltage of the unbiased diode is set to 0 V. The scattering parameters of the two-band tuning mode are shown in Fig. 18(a)-(c). Still, the untuned resonance is marginally affected by the tuning of the other two resonances. However, one can observe a slightly

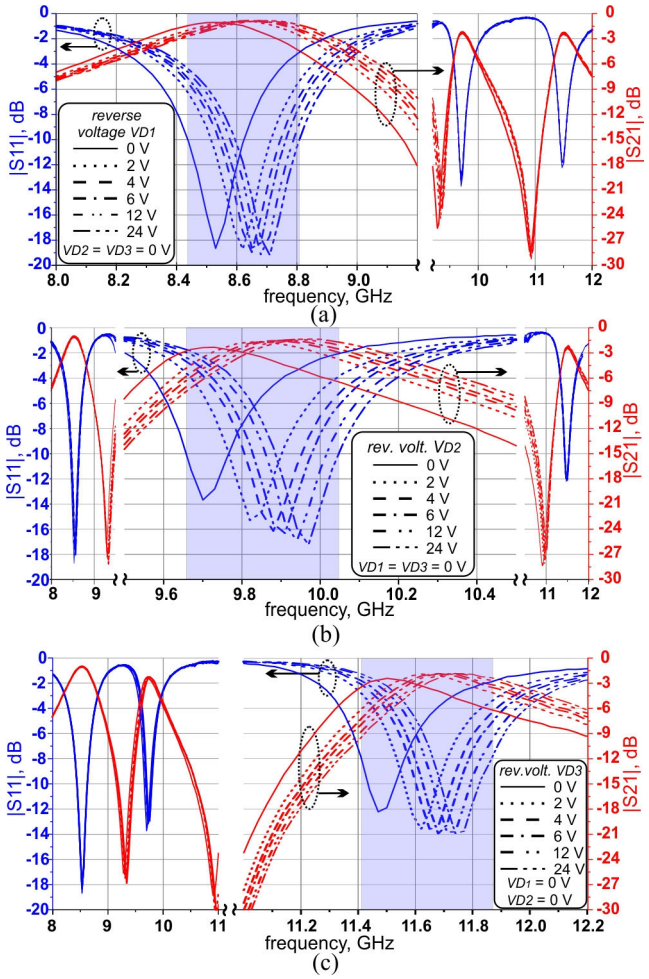

FIGURE 17. Measured scattering parameters of the active diaphragm at the WS for independent band tuning, a) tuning of the lower band, b) tuning of the middle band, and c) tuning of the upper band.

perceptible variation of the untuned second resonance corresponding to the middle ring-slot. This effect can be explained as this middle ring slot experiences a mutual coupling from both the inner and the outer ring-slots.

D. MEASURED AND SIMULATED DATA COMPARISON

The measured data was compared with the simulated results of the AFSS unit cell located in the waveguide's cross-section. Therefore, full wave simulations were obtained using CST Studio Suite for the operating modes reported in subsections *A*, *B* and *C*. Simulated results obtained with the ECM using ADS Keysight are also included.

The same equivalent circuit proposed in section III was used, however some adjustments were considered. Firstly, the value of L_{e1} was reduced to 0.477 nH as the period b of the fabricated unit cell increased. Secondly, the model of the varactor diode is replaced by a series configuration (a capacitance connected in series with a resistance) provided by the diode manufacturer. Finally, the characteristic impedance of the rectangular waveguide is considered in

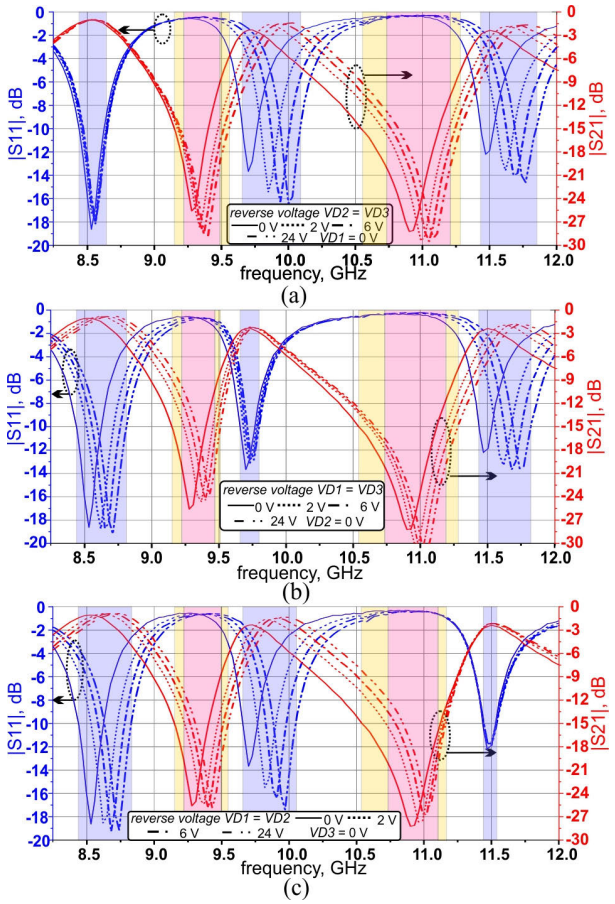

FIGURE 18. Measured scattering parameters of the active diaphragm at the WS for two-band tuning, a) tuning of the middle and upper bands, b) tuning of the lower and upper bands, and c) tuning of the lower and middle bands.

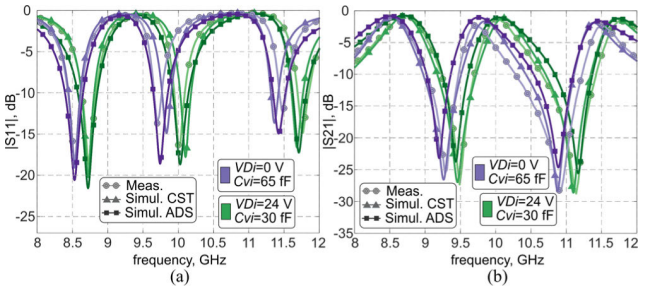

FIGURE 19. Comparison of simulated and measured results in the WS for simultaneous band tuning. a) Reflection coefficient magnitude, and b) transmission coefficient magnitude.

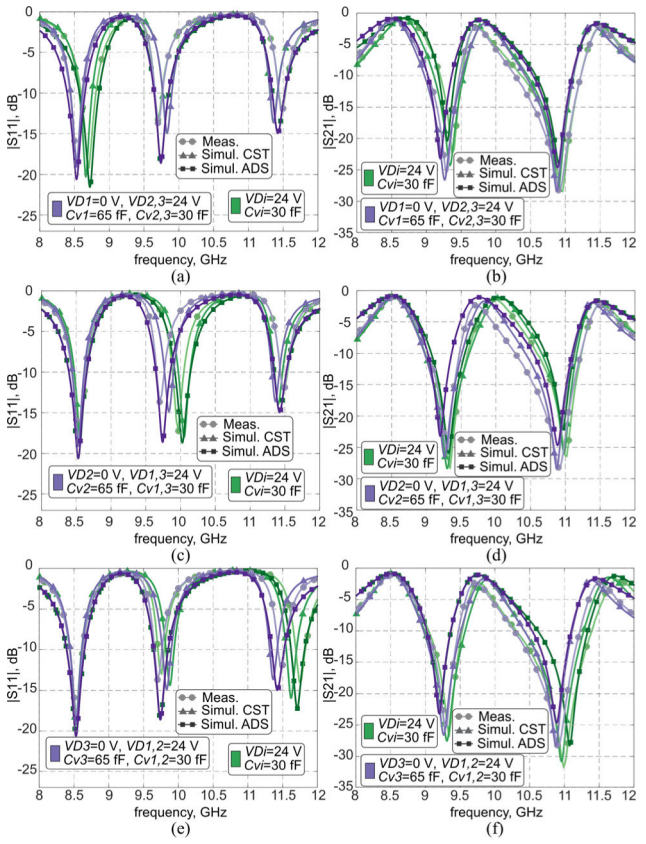

FIGURE 20. Comparison of simulated and measured results in the WS for independent band tuning. Lower band tuning: a) Reflection coefficient magnitude, and b) transmission coefficient magnitude. Middle band tuning: c) Reflection coefficient magnitude, and d) transmission coefficient magnitude. Upper band tuning: e) Reflection coefficient magnitude, and f) transmission coefficient magnitude.

the termination ports. The reference in all subsequent plots (green lines) correspond to the case when all the reverse voltages across the varactor diodes in the measurement are kept constant at 24 V ($V_{D1} = V_{D2} = V_{D3} = 24$ V), which is related to the minimum loading capacitance of 30 fF ($C_{v1} = C_{v2} = C_{v3} = 30$ fF). The variation is shown by plots (purple lines) that correspond to the cases when one or more bias voltages are varied to 0 V, which occurs when all the ring slots are loaded with the maximum varactor's capacitance of 65 fF. According to the manufacturer's data sheet, the series resistance in the varactor's model was set to 1.65 and 3.2 Ω for the varactor's capacitance values of 30 and 65 fF, respectively. Fig. 19(a) and (b) show the reflection coefficient magnitudes $|S_{11}|$ and the transmission coefficient magnitudes $|S_{21}|$, respectively, for the measured and simulated results of the synchronized tuning operating mode described in subsection *A*.

On the other hand, Fig. 20 shows the reflection coefficient magnitudes $|S_{11}|$ and the transmission coefficient magnitudes $|S_{21}|$ for the measured and simulated results of the independent band tuning described in subsection *B*. The first case with loading variation shown in Fig. 20(a-b) corresponds to $V_{D1} = 0$ V, $V_{D2} = 24$ V, $V_{D3} = 24$ V, $C_{v1} = 65$ fF, $C_{v2} = 30$ fF, and $C_{v3} = 30$ fF. The second case shown in Fig. 20(c-d) corresponds to $V_{D1} = 24$ V, $V_{D2} = 0$ V, $V_{D3} = 24$ V, $C_{v1} = 30$ fF, $C_{v2} = 65$ fF, and $C_{v3} = 30$ fF. The third case shown in Fig. 20(e-f) corresponds to $V_{D1} = 24$ V, $V_{D2} = 24$ V, $V_{D3} = 0$ V, $C_{v1} = 30$ fF, $C_{v2} = 30$ fF, and $C_{v3} = 65$ fF.

Next, Fig. 21 shows the comparison of the dual band tuning described in subsection *C*. The first case with loading variation shown in Fig. 21(a-b) corresponds to $V_{D1} = 24$ V,

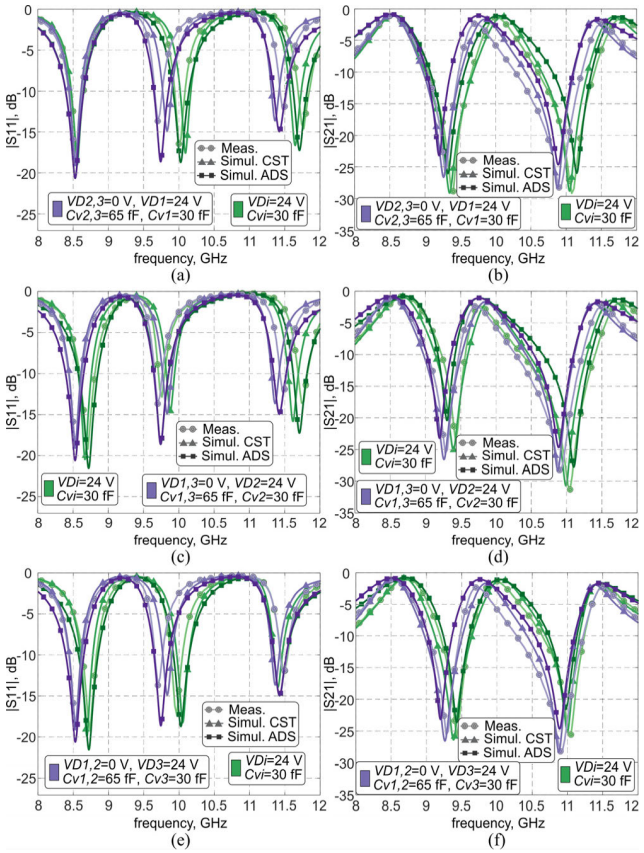

FIGURE 21. Comparison of simulated and measured results in the WS for dual band tuning. Middle and upper band tuning: a) Reflection coefficient magnitude, and b) transmission coefficient magnitude. Lower and upper band tuning: c) Reflection coefficient magnitude, and d) transmission coefficient magnitude. Lower and middle band tuning: e) Reflection coefficient magnitude, and f) transmission coefficient magnitude.

TABLE 4. Comparison with dual-band/tri band tunable AFSSs.

Tunable FSS	Number of bands	Type	Tunable range [GHz]	Frequency ratios of center band frequencies	Unit cell electrical Size*
[33]	2	Bandpass	1.5-2.6 2.2-4	f_2/f_1=1.51	$0.07\lambda_{01}$ $0.10\lambda_{02}$
[34]	3	Bandpass	2930-3130 4520-4660 5790-5970	f_2/f_1=1.28 f_3/f_2=1.51	$0.10\lambda_{01}$ $0.15\lambda_{02}$ $0.20\lambda_{03}$
[35]	2	Bandpass	2.28-4.66 5.44-11.30	f_2/f_1=2.40	$0.05\lambda_{01}$ $0.13\lambda_{02}$
[36]	2	Bandstop	0.28-1.28 0.52-1.98	f_2/f_1=1.60	$0.03\lambda_{01}$ $0.06\lambda_{02}$
This work	3	Bandpass	8.53-8.74 9.70-10.03 11.47-11.77	f_2/f_1=1.14 f_3/f_2=1.18	$0.29\lambda_{01}$ $0.32\lambda_{02}$ $0.38\lambda_{03}$

*with respect to the lowest frequency in the band.

$V_{D2} = 0$ V, $V_{D3} = 0$ V, $C_{v1} = 30$ fF, $C_{v2} = 65$ fF, and $C_{v3} = 65$ fF. The second case shown in Fig. 21(c-d) corresponds to $V_{D1} = 0$ V, $V_{D2} = 24$ V, $V_{D3} = 0$ V, $C_{v1} = 65$ fF, $C_{v2} = 30$ fF, and $C_{v3} = 65$ fF. The third case shown in Fig. 21(e-f) corresponds to $V_{D1} = 0$ V, $V_{D2} = 0$ V, $V_{D3} = 24$ V, $C_{v1} = 65$ fF, $C_{v2} = 65$ fF, and $C_{v3} = 30$ fF. A reasonable agreement between simulated and measured results was obtained. The discrepancies can be attributed to fabrication tolerances and the spread in capacitance values in real varactor diodes.

Finally, the present work is compared in Table 4 with other multiband tunable FSS works reported in the literature. One can observe that with the proposed approach, the frequency ratios of the contiguous center band frequencies are smaller than other previous works, ensuring the close band operation of the multiband FSS.

VI. CONCLUSION

In this paper, a triband AFSS unit cell based on concentric loaded split ring slots with independent band tuning using the third resonant mode has been investigated in this paper. The novelty is the usage of the third resonant mode of the split ring slot resonators, instead of the fundamental resonant mode, for a tunable multiband AFSS with closely spaced frequencies. This third mode allows the reduction of the mutual coupling between the densely packed resonators to ensure independent band tuning. The reactive loading with varactor diodes at the proper locations within the split ring slots ensures the efficient tuning capability of the AFSS. The design of the required conducting paths for biasing the three active devices independently in the unit cell allows low disruption in microwave frequencies. As a result, a triple band AFSS unit cell based on varactor-loaded split ring slots, optimized for independent band tuning operation and close band response was presented. The operation of an active diaphragm with independent band tuning capabilities in X-band has been demonstrated. Unbiased varactor diodes provide resonant frequencies at 8.53, 9.70 and 11.47 GHz with insertion loss of 1.1, 2.3 and 2.4 dB, respectively, while the reverse-biased diodes with maximum voltages ensure resonant frequencies at 8.74, 10.03 and 11.77 GHz with insertion loss of 0.8, 1.4 and 1.7 dB, respectively. Tuning ranges of 210, 330 and 300 MHz for the first, second and third resonant frequencies were obtained, respectively. The -10 dB reflection coefficient bandwidth for the first, second and third bands are 495, 436 and 418 MHz, respectively. Close band response was also achieved with frequency band ratios of 1.18 and 1.14 for the third to the second resonance, and for the second to the first resonance, respectively. It is shown that the proposed tunable triband AFSS unit cell has good performance in terms of close band spacing and frequency tunability with reasonable levels of transmission loss.

REFERENCES

[1] B. A. Munk, *Frequency Selective Surfaces: Theory and Design*. New York, NY, USA: Wiley, 2000.

[2] T. K. Wu, *Frequency Selective Surfaces and Grid Arrays*. New York, NY, USA: Wiley, 1995.

[3] L. Zhang, G. Yang, Q. Wu, and J. Hua, "A novel active frequency selective surface with wideband tuning range for EMC purpose," *IEEE Trans. Magn.*, vol. 48, no. 11, pp. 4534–4537, Nov. 2012.

[4] M. Bouslama, M. Traii, T. A. Denidni, and A. Gharsallah, "Reconfigurable frequency selective surface for beam-switching applications," *IET Microw., Antennas Propag.*, vol. 11, no. 1, pp. 69–74, Jan. 2017.

[5] R. Sivasamy, B. Moorthy, M. Kanagasabai, V. R. Samsingh, and M. G. N. Alsath, "A wideband frequency tunable FSS for electromagnetic shielding applications," *IEEE Trans. Electromagn. Compat.*, vol. 60, no. 1, pp. 280–283, Feb. 2018.

[6] Y. Li, P. Ren, and Z. Xiang, "A dual-passband frequency selective surface for 5G communication," *IEEE Antennas Wireless Propag. Lett.*, vol. 18, no. 12, pp. 2597–2601, Dec. 2019.

[7] S. Qiu, Q. Guo, and Z. Li, "Tunable frequency selective surface based on a sliding 3D-printed inserted dielectric," *IEEE Access*, vol. 9, pp. 19743–19748, 2021.

[8] B. Döken and M. Kartal, "Triple band frequency selective surface design for global system for mobile communication systems," *IET Microw., Antennas Propag.*, vol. 10, no. 11, pp. 1154–1158, Aug. 2016.

[9] M. Yan, J. Wang, H. Ma, M. Feng, Y. Pang, S. Qu, J. Zhang, and L. Zheng, "A tri-band, highly selective, bandpass FSS using cascaded multilayer loop arrays," *IEEE Trans. Antennas Propag.*, vol. 64, no. 5, pp. 2046–2049, May 2016.

[10] M. Kartal, J. J. Golezani, and B. Doken, "A triple band frequency selective surface design for GSM systems by utilizing a novel synthetic resonator," *IEEE Trans. Antennas Propag.*, vol. 65, no. 5, pp. 2724–2727, May 2017.

[11] N. Liu, X. Sheng, C. Zhang, J. Fan, and D. Guo, "A miniaturized triband frequency selective surface based on convoluted design," *IEEE Antennas Wireless Propag. Lett.*, vol. 16, pp. 2384–2387, 2017.

[12] S. Yadav, C. P. Jain, and M. M. Sharma, "Smartphone frequency shielding with penta-bandstop FSS for security and electromagnetic health applications," *IEEE Trans. Electromagn. Compat.*, vol. 61, no. 3, pp. 887–892, Jun. 2019.

[13] A. Dey and R. Sanyal, "Single layer miniaturized ultra-thin FSS with five closely spaced bands," *Int. J. Microw. Wireless Technol.*, vol. 11, no. 8, pp. 797–805, Oct. 2019.

[14] S. Monni, A. Neto, G. Gerini, F. Nennie, and A. Tijhuis, "Frequency-selective surface to prevent interference between radar and SATCOM antennas," *IEEE Antennas Wireless Propag. Lett.*, vol. 8, pp. 220–223, 2009.

[15] P. S. Taylor, A. C. M. Austin, E. A. Parker, M. J. Neve, J. C. Batchelor, J. T.-P. Yiin, M. Leung, G. B. Rowe, A. G. Williamson, and K. W. Sowerby, "Angular independent frequency selective surfaces for interference control in indoor wireless environments," *Electron. Lett.*, vol. 48, no. 2, pp. 61–62, Jan. 2012.

[16] R. Saleem, M. Bilal, H. T. Chattha, S. U. Rehman, A. Mushtaq, and M. F. Shafique, "An FSS based multiband MIMO system incorporating 3D antennas for WLAN/WiMAX/5G cellular and 5G Wi-Fi applications," *IEEE Access*, vol. 7, pp. 144732–144740, Oct. 2019.

[17] R. R. Xu, H. C. Zhao, Z. Y. Zong, and W. Wu, "Dual-band capacitive loaded frequency selective surfaces with close band spacing," *IEEE Microw. Wireless Compon. Lett.*, vol. 18, no. 12, pp. 782–784, Dec. 2008.

[18] C.-N. Chiu and W.-Y. Wang, "A dual-frequency miniaturized-element FSS with closely located resonances," *IEEE Antennas Wireless Propag. Lett.*, vol. 12, pp. 163–165, 2013.

[19] F.-C. Huang, C.-N. Chiu, T.-L. Wu, and Y.-P. Chiou, "Very closely located dual-band frequency selective surfaces via identical resonant elements," *IEEE Antennas Wireless Propag. Lett.*, vol. 14, pp. 414–417, 2015.

[20] S. Ghosh and K. V. Srivastava, "An angularly stable dual-band FSS with closely spaced resonances using miniaturized unit cell," *IEEE Microw. Wireless Compon. Lett.*, vol. 27, no. 3, pp. 218–220, Mar. 2017.

[21] S. B. Paiva, V. P. S. Neto, and A. G. D'Assuncao, "A new compact, stable, and dual-band active frequency selective surface with closely spaced resonances for wireless applications at 2.4 and 2.9 GHz," *IEEE Trans. Electromagn. Compat.*, vol. 62, no. 3, pp. 691–697, Jun. 2020.

[22] G. Shah, Q. Cao, Z. U. Abidin, and Z. Rafique, "A hybrid element triband frequency selective surface with high angular stability and polarization insensitivity," *IEEE Trans. Electromagn. Compat.*, vol. 62, no. 6, pp. 2759–2764, Dec. 2020.

[23] H. Fabian-Gongora, A. E. Martynyuk, J. Rodriguez-Cuevas, and J. I. Martinez-Lopez, "Active dual-band frequency selective surfaces with close band spacing based on switchable ring slots," *IEEE Microw. Wireless Compon. Lett.*, vol. 25, no. 9, pp. 606–608, Sep. 2015.

[24] H. Fabian-Gongora, A. E. Martynyuk, J. Rodriguez-Cuevas, and J. I. Martinez-Lopez, "Closely spaced tri-band frequency selective surfaces based on split ring slots," *Electron. Lett.*, vol. 52, no. 9, pp. 727–729, Apr. 2016.

[25] J. M. Zendejas, J. P. Gianvittorio, Y. Rahmat-Samii, and J. W. Judy, "Magnetic MEMS reconfigurable frequency-selective surfaces," *J. Microelectromech. Syst.*, vol. 15, no. 3, pp. 613–623, Jun. 2006.

[26] M. Safari, C. Shafai, and L. Shafai, "X-band tunable frequency selective surface using MEMS capacitive loads," *IEEE Trans. Antennas Propag.*, vol. 63, no. 3, pp. 1014–1021, Mar. 2015.

[27] L. Boccia, I. Russo, G. Amendola, and G. D. Massa, "Tunable frequency-selective surfaces for beam-steering applications," *Electron. Lett.*, vol. 45, no. 24, pp. 1213–1215, Nov. 2009.

[28] I. Gil, J. Bonache, J. Garcia-Garcia, and F. Martin, "Tunable metamaterial transmission lines based on varactor-loaded split-ring resonators," *IEEE Trans. Microw. Theory Techn.*, vol. 54, no. 6, pp. 2665–2674, Jun. 2006.

[29] A. L. Borja, J. Carbonell, J. D. Martinez, V. E. Boria, and D. Lippens, "A controllable bandwidth filter using varactor-loaded metamaterial-inspired transmission lines," *IEEE Antennas Wireless Propag. Lett.*, vol. 10, pp. 1575–1578, 2011.

[30] D. K. Choudhary and R. K. Chaudhary, "A compact CPW-based dual-band filter using modified complementary split ring resonator," *AEU Int. J. Electron. Commun.*, vol. 89, pp. 110–115, May 2018.

[31] D. K. Choudhary and R. K. Chaudhary, "Compact lowpass and dual-band bandpass filter with controllable transmission zero/center frequencies/passband bandwidth," *IEEE Trans. Circuits Syst. II, Exp. Briefs*, vol. 67, no. 6, pp. 1044–1048, Jun. 2020.

[32] R. P. Jenkins, M. D. Gregory, L. Cardillo, B. R. Bunes, S. D. Campbell, P. L. Werner, and D. H. Werner, "A low-power tunable frequency selective surface for multiplexed remote sensing," *IEEE Access*, vol. 9, pp. 58478–58486, 2021.

[33] B. Sanz-Izquierdo, E. A. Parker, and J. C. Batchelor, "Dual-band tunable screen using complementary split ring resonators," *IEEE Trans. Antennas Propag.*, vol. 58, no. 11, pp. 3761–3765, Nov. 2010.

[34] D.-W. Wang, W.-S. Zhao, H. Xie, J. Hu, L. Zhou, W. Chen, P. Gao, J. Ye, Y. Xu, H.-S. Chen, E.-P. Li, and W.-Y. Yin, "Tunable THz multiband frequency-selective surface based on hybrid metal–graphene structures," *IEEE Trans. Nanotechnol.*, vol. 16, no. 6, pp. 1132–1137, Nov. 2017.

[35] Y. Rahmani-Shams, S. Mohammd-Ali-Nezhad, A. N. Yeganeh, and S. H. Sedighy, "Dual band, low profile and compact tunable frequency selective surface with wide tuning range," *J. Appl. Phys.*, vol. 123, no. 23, Jun. 2018, Art. no. 235301.

[36] S. Ghosh and K. V. Srivastava, "A dual-band tunable frequency selective surface with independent wideband tuning," *IEEE Antennas Wireless Propag. Lett.*, vol. 19, no. 10, pp. 1808–1812, Oct. 2020.

[37] M. Vaccarono, V. Chandrasekar, R. Bechini, and R. Cremonini, "Origin and nature of electromagnetic interference in X-band weather radars," in *Proc. URSI Asia–Pacific Radio Sci. Conf. (AP-RASC)*, New Delhi, India, Mar. 2019, p. 1.

[38] A. D. Chuprin, E. A. Parker, and J. C. Batchelor, "Resonant frequencies of open and closed loop frequency selective surface arrays," *Electron. Lett.*, vol. 36, no. 19, pp. 1601–1603, Sep. 2000.

[39] A. E. Martynyuk, A. G. Martinez-Lopez, and J. I. Martinez-Lopez, "2-bit X-band reflective waveguide phase shifter with BCB-based bias circuits," *IEEE Trans. Microw. Theory Techn.*, vol. 54, no. 12, pp. 4056–4061, Dec. 2006.

[40] R. Martinez-Lopez, J. Rodriguez-Cuevas, A. E. Martynyuk, and J. I. Martinez-Lopez, "Miniaturized frequency-selective surfaces based on monolithically integrated components," *IEEE Trans. Antennas Propag.*, vol. 68, no. 6, pp. 4668–4676, Jun. 2020.

[41] H. A. Wheeler, "The radiation resistance of an antenna in an infinite array or waveguide," *Proc. IRE*, vol. 36, no. 4, pp. 478–487, Apr. 1948.

[42] P. W. Hannan, P. J. Meier, and M. A. Balfour, "Simulation of phased array antenna impedance in waveguide," *IEEE Trans. Antennas Propag.*, vol. AP-11, no. 6, pp. 715–716, Nov. 1963.

HENRY FABIAN-GONGORA was born in Veracruz, Mexico. He received the B.S. degree in electronics engineering from the Technological Institute of Veracruz, in 2009, and the M.Eng. and Ph.D. degrees in electrical engineering from the National Autonomous University of Mexico (UNAM), Mexico City, in 2014 and 2018, respectively. Since 2019, he has been a Professor with the School of Engineering, Autonomous University of Campeche (UAC). His current research interests include frequency selective surfaces, meta-surfaces, antenna arrays, and microwave circuits.

ALEXANDER E. MARTYNYUK was born in Kiev, Ukraine. He received the M.Sc. degree in radio engineering and the Ph.D. degree from the Kyiv Polytechnic Institute, Kiev, in 1988 and 1993, respectively. From 1988 to 1995, he was with the Faculty of Radio Engineering, Kyiv Polytechnic Institute. Since 1995, he has been with the National Autonomous University of Mexico (UNAM), Mexico City, Mexico. He is currently a Professor with the School of Engineering, UNAM. His research interests include microwave and millimeter-wave devices, antenna arrays, and millimeter-wave communications.

JORGE RODRIGUEZ-CUEVAS was born in Mexico City, Mexico. He received the B.S., M.Eng., and Ph.D. degrees in electrical engineering from the National Autonomous University of Mexico (UNAM), Mexico City, in 1987, 1995, and 2003, respectively. He also received specialized studies in micro-electromechanical systems (MEMS) from UNAM and the United States-Mexico Foundation for Science (FUMEC), Mexico City, in 2003. Since 1987, he has been with the Electronics Engineering Department, UNAM, where he is currently a Professor engaged in research and teaching on telecommunication circuits and systems. His current research interests include phased arrays, RF MEMS, and microwave and millimeter-wave circuits.

LOURDES MARTINEZ-LOPEZ was born in Mexico City, Mexico. She received the B.S., M.Eng., and Ph.D. degrees in electrical engineering from the National Autonomous University of Mexico (UNAM), Mexico City, in 2006, 2008, and 2015, respectively. She is currently a Professor of electrical engineering with UNAM. Her current research interests include circular polarizers, frequency selective surfaces, meta-surfaces, and antenna arrays.

ROSALBA MARTINEZ-LOPEZ was born in Mexico City, Mexico. She received the B.S. degree in computer engineering, and the M.Eng. and Ph.D. degrees in electrical engineering from the National Autonomous University of Mexico (UNAM), Mexico City, in 2004, 2007, and 2013, respectively. Since 2013, she has been a Professor with the School of Engineering, UNAM. Her current research interests include frequency selective surfaces, micro-electromechanical systems (MEMS), antenna arrays, and microwave circuits.

JOSE I. MARTINEZ-LOPEZ (Member, IEEE) was born in Mexico City, Mexico. He received the B.S., M.Eng., and Ph.D. degrees in electrical engineering from the National Autonomous University of Mexico (UNAM), Mexico City, in 1994, 1998, and 2005, respectively. In 2006, he was with the Schlumberger Technology Center, Sugar Land, TX, USA, where he was developing antennas for deep induction array tools for the oil industry. In 2009, he was a Visiting Scholar with the Electroscience Laboratory, The Ohio State University (OSU), Columbus, OH, USA. He is currently a Professor of electrical engineering with UNAM. He is also on a sabbatical leave as a Visiting Scholar with the Nonlinear RF Laboratory, Department of Electrical and Computer Engineering (ECE), OSU. His current research interests include antenna arrays, frequency selective surfaces, and microwave and millimeter-wave circuits.